Renewable Energy 216 (2023) 119043

Contents lists available at ScienceDirect

Renewable Energy

journal homepage: www.elsevier.com/locate/renene

A regional solar forecasting approach using generative adversarial networks with solar irradiance maps

Haoran Wen [a], Yang Du [b,*], Xiaoyang Chen [a], Eng Gee Lim [a], Huiqing Wen [a], Ke Yan [c]

[a] School of Advanced Technology, Xi'an Jiaotong-Liverpool University, China
[b] College of Science and Engineering, James Cook University, Australia
[c] College of Mechanical and Vehicle Engineering, Hunan University, China

ARTICLE INFO

Keywords:
Regional solar forecasting
Solar irradiance map
Generative adversarial network
PV estimation

ABSTRACT

The intermittent and stochastic nature of solar resource hinders the integration of solar energy into modern power system. Solar forecasting has become an important tool for better photovoltaic (PV) power integration, effective market design, and reliable grid operation. Nevertheless, most existing solar forecasting methods are dedicated to improving forecasting accuracy at site-level (e.g. for individual PV power plants) regardless of the impacts caused by the accumulated penetration of distributed PV systems. To tackle with this issue, this article proposes a novel generative approach for regional solar forecasting considering an entire geographical region of a flexible spatial scale. Specifically, we create solar irradiance maps (SIMs) for solar forecasting for the first time by using spatial Kriging interpolation with satellite-derived solar irradiance data. The sequential SIMs provide a comprehensive view of how solar intensity varies over time and are further used as the inputs for a multi-scale generative adversarial network (GAN) to predict the next-step SIMs. The generated SIM frames can be further transformed into PV power output through a irradiance-to-power model. A case study is conducted in a 24 × 24 km area of Brisbane to validate the proposed method by predicting of both solar irradiance and the output of behind-the-meter (BTM) PV systems at unobserved locations. The approach demonstrates comparable accuracy in terms of solar irradiance forecasting and better predictions in PV power generation compared to the conventional forecasting models with a highest average forecasting skill of 10.93 ± 2.35% for all BTM PV systems. Thus, it can be potentially used to assist solar energy assessment and power system control in a highly-penetrated region.

1. Introduction

1.1. Background

Solar energy is one of the most viable alternatives to fossil fuels because it is environmentally friendly and inexhaustible [1]. However, the intermittent and stochastic nature of the solar resource inhibits optimal utilization of solar energy and poses challenges to power grids [2]. PV power generation is highly dependent on the changes in solar irradiance, i.e., (1) deterministic variability induced by the rotation of the earth and its orbital movement around the sun, and (2) the stochastic variability caused by atmospheric processes such as cloud transients. For the former one, solar irradiance demonstrates predictable diurnal and seasonal trends as shown in Fig. 1(a) and (b). For example, during summer the sun's angle is highest when the northern hemisphere is tilted towards the sun. Thus, the sun provides more energy to the earth's surface and the average solar irradiation is higher than that in other seasons. Similarly, solar irradiation also shows a diurnal trend which is resulted from the rotation of the earth.

For the latter one, solar irradiance becomes non-stationary due to its more stochastic and rapidly changing behaviors caused by moving clouds. This cloud-induced intermittency can cause the so-called partial shading effect in PV systems, which further results in frequency imbalance, voltage limit violation, and malfunction of protection devices, especially for those areas with high PV penetrations [3]. Recently, there has been a substantial upsurge in the expansion of small-scale distributed PV systems that operate behind the meter (BTM). From the perspective of grid operators, these PV power generators are "invisible", signifying that their power productions are not systematically monitored in real-time at the operational level of the power grid. Nonetheless, the electricity generated by these units effectively counterbalances the power requirements of consumers, consequently altering the overall profile of the net electrical load [4]. As the accumulation of

* Corresponding author.
E-mail address: Yang.du@jcu.edu.au (Y. Du).

https://doi.org/10.1016/j.renene.2023.119043
Received 25 October 2022; Received in revised form 1 June 2023; Accepted 14 July 2023
Available online 18 July 2023

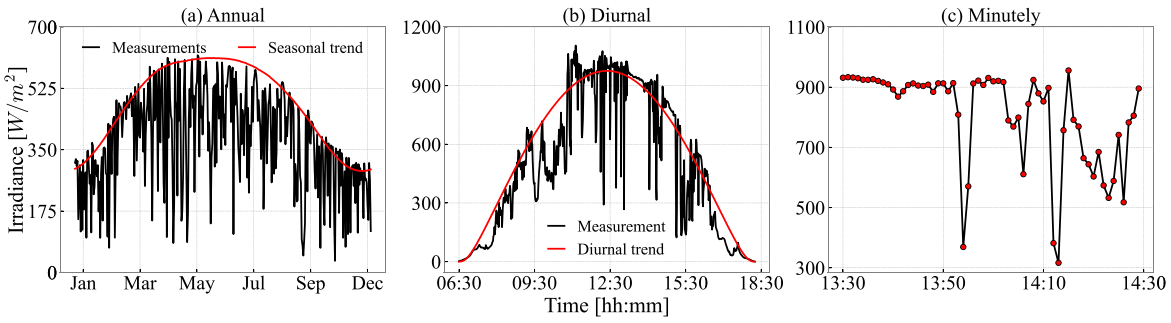

Fig. 1. Solar irradiance variability: (a) seasonal variation with daily averaged values, (b) diurnal variation with minutely values on 2018 April 12 at Golden, Colorado, and (c) a zoomed view from 13:30 to 14:30 pm on the same day. The data is obtained from the National Renewable Energy Laboratory (NREL) Baseline Measurement System [6].

BTM PV capacity increases, it is crucial to forecast BTM PV power production to maintain a balance between power supply and demand [5]. Therefore, reliable and accurate forecasts and estimation of distributed PV power production and solar resource are required for better power system operation and solar utilization.

1.2. Related works

In a symbiotic relationship to the development of solar energy technology, solar forecasting has become one of the most prominent topics in the field [7]. However, most of the existing studies are dedicated to forecasting the output power of individual PV power plants, where the production measurements and local weather data at the site are available. There is still a limited number of works focus on the estimation of the regional power production of distributed PV systems.

1.2.1. Regional solar forecasting

Regional solar forecasting is referred to as the forecasts of the amount of solar irradiance or PV power generation that will be available in a specific region or area over a period of time. The range of an interested region can vary depending on the density of PV installations, grid infrastructure, weather patterns, and the specific objectives of the forecasting applications. The forecasting approaches for regional PV power can be grouped into *bottom-up* and *upscaling* approaches, based on the availability of the requisite PV system data [8].

The bottom-up forecasting involves predicting PV power generation in a given area by aggregating the predictions for individual PV sites. This method is particularly suitable for aggregating all individual PV power systems when their specifications are known (e.g., the location and capacity) and understanding the localized effects in regional analyses. As discussed in [9], regional PV power production can be estimated by predicting each PV installation in the interested region with well-defined physical models combined with irradiance and weather data. Similarly, the California Independent System Operator (ISO) collected all the PV power data and combined it with high-resolution irradiance and weather forecasts data to estimate the total contribution of the distributed PV systems in its grid [10]. In [11], the researchers used clustering and blending strategies to group PV systems with similar weather and geographical conditions into clusters. Then they used the analog ensemble model to predict regional PV power based on the assumption that the PV systems in each cluster share identical solar irradiance and other parameters. This approach offers the advantage of explicitly considering the unique characteristics of each system. However, it presents challenges in the context of distributed PV forecasting, as the availability of PV system data is often limited or incomplete.

In contrast, the upscaling approach is more suitable for the scenario where only partial PV power data are known, e.g., the data from selected representative PV systems can be used to estimate the total generation of the region [12]. Lorenz et al. [13] employed physical models and upscaling techniques to generate regional PV point forecasts for a forecast horizon up to 2 days ahead, aiming to provide accurate predictions of PV power output at a regional level. To employ this approach effectively, it is crucial to carefully select a subset of PV systems and conduct comparisons with metered data on a statistically significant number of sites as benchmarks. This ensures accurate and reliable assessments of the forecasted performance. The problem of poor representation is considered in [14,15], where the data from a large sample of PV systems has been fed into PV models. In [16], fuzzy confidence intervals are employed to handle uncertainties in the input data. This approach offers the advantage of gathering data from a limited number of locations within the region, rather than requiring continuous monitoring of all locations.

In cases where specific data for individual systems is unavailable but aggregated regional PV power data is accessible, it is possible to treat regional forecasting as a simple time series forecasting task by directly predicting the aggregated PV power generation data using statistical models. For example, in [17], the provincial electricity energy generation data can be obtained from the open data portal of the Spanish regulator Red Eléctrica Española. The authors utilize deep neural networks to estimate multiple conditional quantiles on regional renewable electricity production with gridded NWP variables covering the region of interest. If no data is available for either individual PV systems or the region, solar irradiance forecasts can be transformed to power based on the estimated installed capacity [18]. For instance, Lorenz et al. [19] introduced a methodology that effectively predicts solar irradiance based on weather forecasts, enabling its application in the regional forecasting of PV power output for 11 sites located in Germany.

Apart from the methods using PV power data and weather forecasts, image-based models can be used to assess solar energy resources using satellite remote sensing data. A study uses a Geographic Information System (GIS) tool to generate solar radiation maps to evaluate monthly and yearly solar radiation distribution for the first time in Oman, which helps policymakers to efficiently establish a viable solar energy market [20]. Besides, solar power maps are produced by using a small set of metered PV systems in [21], and can then be used in conjunction with other data sources (such as weather data or satellite imagery) for more accurate forecasting of the total distributed solar PV generation of an entire region. Nonetheless, the quality of solar power maps largely depends on the distribution and density of PV power plants. For regions with sparse or unobserved PV systems, it is difficult to generate solar power maps that can accurately describe PV production.

1.2.2. Generative solar forecasting

Supported by the recent development of computational hardware and the exponential growth of available data, deep learning (DL) has achieved great success in many industrial and academic fields. In the solar community, researchers have also utilized DL models such as recurrent neural networks (RNNs) for solar forecasting, i.e., making forecasts by processing sequential data and learning temporal dependencies in time series. Recently, generative models, e.g., generative

adversarial network (GAN) architecture, are employed in solar forecasting. Unlike the RNNs, the underlying principle of the generative approaches is to learn data distribution of training data and try to generate data following that distribution. Thus, GAN models are used to generate synthesized solar irradiance or PV power data to facilitate training other DL models. For example, Jiang et al. Wang et al. [22] used a GAN to generate training data for weather classification and day-head PV power prediction and Khodayar et al. [23] proposed a scalable GAN to generate data samples from the probability densities obtained from each node of a graph. Debnath et al. [24] introduced a time-series data augmentation method to address the data scarcity problem in multi-variate solar forecasting. In [25], the author used GANs to model uncertainties in different forecasting scenarios for stochastic PV power generation.

Besides, GANs can be also combined with other forecasting to enhance forecasting performance [26,27]. Huang et al. [26] proposed a time series forecasting based on CGANs. The main contribution of this work lies in the modification of the generator, in which the convolutional layers are replaced by a regression model (i.e., Conv1D) for temporal feature extraction and a Bi-LSTM for making predictions. Similarly, the discriminator compares the prediction (fake) and the ground truth (real) for improving the generator. In [28], the authors first use a wavelet transform package to decompose the GHI time series into sub-frequency signals. Then GANs are used as the forecasting models for each sub-signal and the predictions for each sub-signal are reconstructed. Instead of using back-propagation, an evolutionary algorithm based on the dragonfly algorithm is used as the training method, which is further optimized by a three-phase adaptive modification. In addition to time series, the generative architectures also demonstrate powerful ability in image-based forecasting. In [29], the authors use the GAN model to combine with other pre-processing techniques to predict annual hourly solar irradiance on building facades using fish-eye images. In [30], cloud coverage can be predicted by producing the future frames of a sky image sequence with GAN. Nevertheless, the clouds are highly deformable objects with continuously changing shapes and difficulties still exist in the estimation of clouds and the conversion from sky images to ground-projected shadows and irradiance. These works are still dedicated to improving site-specific forecasting accuracy without addressing the problems in forecasts at regional levels.

1.3. Contributions

In light of the above motivations, a novel generative approach is proposed to predict regional solar irradiance variation for estimating distributed PV power production. This method uses spatial Kriging to generate image-based input data, namely solar irradiance maps (SIMs) with satellite-derive irradiance data. Then a pre-trained multi-scale GAN generates next-step SIMs from an input sequence of the previous 5 frames. The predicted SIMs frames can be further transformed into individual PV power outputs at any location in the region, thus making it particularly suitable for the utilities to estimate unobserved PV systems. To the best of our knowledge, this is the first work that uses GAN for regional solar forecasting. In light of the above, the scientific contributions of this study can be summarized as follows:

- This paper proposes a generative forecasting approach for solar irradiance at the regional level where conventional methods struggle. It extends forecasts of small areas to regional forecasts by generating the solar profile of an entire region of flexible geographical scale and spatial resolution.
- Unlike other generative approaches trained on time series, we create a new image-based data source for the generative forecasting model, i.e. SIMs, which provide an intuitive and visualized view of how solar irradiance varies at a regional level. The sequential SIMs are created by interpolating the gridded satellite-derived irradiance time series which contains both temporal and spatial information.
- Last but not least, the predicted SIMs can be used for estimating the distributed PV power in that region. It enables forecasts of individual PV output by extracting the predicted irradiance time series at any geographical location and converting it to PV data with an irradiance-to-power conversion model. A case study is provided to verify the effectiveness of our approach on real-world PV output data, making it promising for practical applications.

The remainder of this paper is organized as follows. Section 2 describes the data for the experiment. Section 3 introduced the proposed solar forecasting approach with a detailed explanation. Section 4 presents the experiment results with discussions, followed by the conclusion and future work in Section 5.

2. Data description

2.1. Solar irradiance data

Publicly available and high-quality solar resource data is fundamental and crucial for solar technologies. It enables accurate predictions of PV system output and facilitates the deployment of solar energy technologies in PV systems. The NSRDB is a comprehensive compilation of hourly and half-hourly data, including the three primary solar radiation measurements, namely global horizontal irradiance (GHI), direct normal irradiance (DNI), and diffuse horizontal irradiance (DHI), along with accompanying meteorological data [31]. The current version of NSRDB is constructed by modeling techniques utilizing multi-channel measurements obtained from geostationary satellites, whereas earlier versions relied on cloud and weather data sourced primarily from airports. The inclusion of an sufficient number of geographically diverse locations, as well as meticulous consideration of temporal and spatial scales, ensures accurate representation of regional solar radiation climates in the NSRDB.

There are two commonly applied methods for obtaining solar resource data from models: (a) an empirical approach that correlates ground-based observations with satellite measurements, and (b) a physics-based approach that considers the radiation received at the satellite and generates retrievals to estimate clouds and surface radiation. While empirical methods have traditionally been used for calculating surface radiation, the advancement of faster computing has made physical models feasible [32]. The Physical Solar Model (PSM) developed by NREL computes GHI using visible and infrared channel measurements from the Geostationary Operational Environmental Satellites (GOES) system. The current NSRDB contains multiple datasets with various spatial and temporal resolutions. The data is generated by an improved version of PSM V3 and shows better correlation with the ground-measured data [33].

In this article, we use the dataset covering Asia, Australia, and Pacific regions with a 2 km × 2 km, 10-min resolution from 2018–2020. The data is regularly gridded with a spatial resolution of approximately 0.02° in both latitude and longitude. Particularly, a 24 × 24 km^2 area in Brisbane shown in Fig. 2(a), which is located between Latitudes 27.36° and 27.58° South and Longitudes 152.91° and 153.15° East, is chosen as the interested region for forecasting due to the high penetration of distributed PV systems. In this region, there are 156 solar irradiance measurement points (red dots) evenly located in this region with a spatial resolution of 2 km as shown in Fig. 2(b). We use 2018–2019 data as the training set and 2020 data for out-of-sample testing. Besides, the zero values during the night are removed and diurnal values from 06:00 to 18:00 are preserved. Fig. 2(c) shows an example of the satellite derived GHI at one of the locations.

To remove the diurnal trend of solar irradiance data, we use the clear-sky index (CSI) for generating SIMs instead of directly using GHI values. This step is very important for generating SIMs because it ensure consistency of SIMs regarding "clearness" rather than solar irradiance

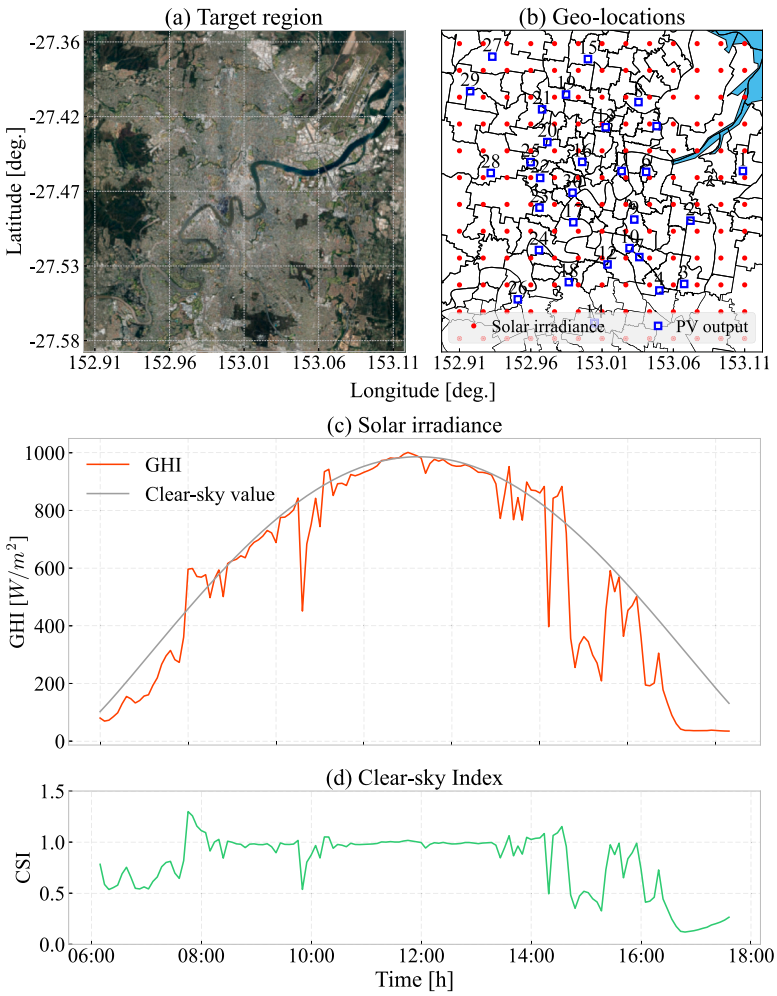

Fig. 2. The target area in Brisbane, Australia: (a) satellite imagery, (b) geographic locations of data points. The red dots indicate the locations where solar irradiance are available (observed) and the blue squares are the BTM PV systems for estimation (unobserved), (c) daily solar irradiance variation at an observed location, and (d) the corresponding CSI values.

intensity. The CSI is defined as the ratio between the measured irradiance (I) and clear-sky irradiance (I_{cs}) under a clear-sky atmosphere:

$$\text{CSI} = \frac{\text{measured GHI}}{\text{clear-sky GHI}} \tag{1}$$

where the clear-sky GHI values are calculated by using Ineichen–Perez clear-sky model [34] that considers Linke turbidity. Since there are overshoot GHI values which make CSI abnormally high, we limit CSI values at a range of (0, 1.2] to reduce unexpected predictions. An example of corresponding CSI is shown in Fig. 2(d).

2.2. PV output data

To validate the effect of the method, we utilize the forecasting results for BTM PV power estimation. The PV output data are obtained from *PVOutput.org*, which is a widely-used online platform that allows users to track and share PV system performance data in real-time. This article leverages the wealth of the data for empirical research to investigate and evaluate the regional BTM PV power production across different geographical locations, system sizes, and environmental conditions. In this sense, we selected 30 PV systems of capacities from 4 kW to 13.08 kW in this area for validation and demonstration purposes. Fig. 2(b) shows the geographic distribution of the selected PV systems (blue squares) based on their coordination information.

3. Methodology

3.1. The proposed regional solar forecasting framework

Unlike conventional solar forecasting methods that forecast future solar irradiance at a single location, the objective of the proposed forecasting framework is to predict solar radiation of an entire region by generating further SIMs without exogenous variables. Fig. 3 illustrates a general process of the proposed regional solar forecasting framework. It consists of three stages: (1) data processing and SIM generation, (2) adversarial training and forecasting, and (3) irradiance-to-power conversion.

3.2. Creating SIMs using spatial kriging

In the first stage, we create solar irradiance maps using kriging interpolation. Creating SIMs for a certain region entails creating graphics that depict the geographical distribution of solar irradiance intensity across that area. Kriging is a weighted interpolation method based on a geostatistical process that produces an estimated surface from a set of measured points. It assumes that the distance or direction between sample points reflects a spatial correlation and determines the values for unknown locations.

Given solar irradiance time series $\boldsymbol{I}(t)$ at a set of locations $\mathbf{s} \in \mathbb{R}^d$, the spatial–temporal relation of the solar irradiance observations in the

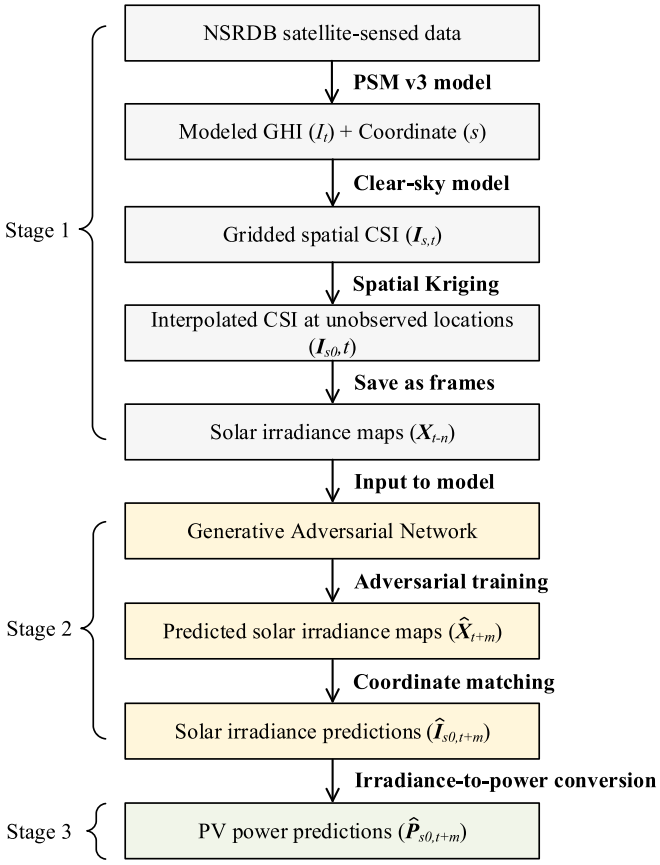

Fig. 3. The proposed regional solar forecasting framework.

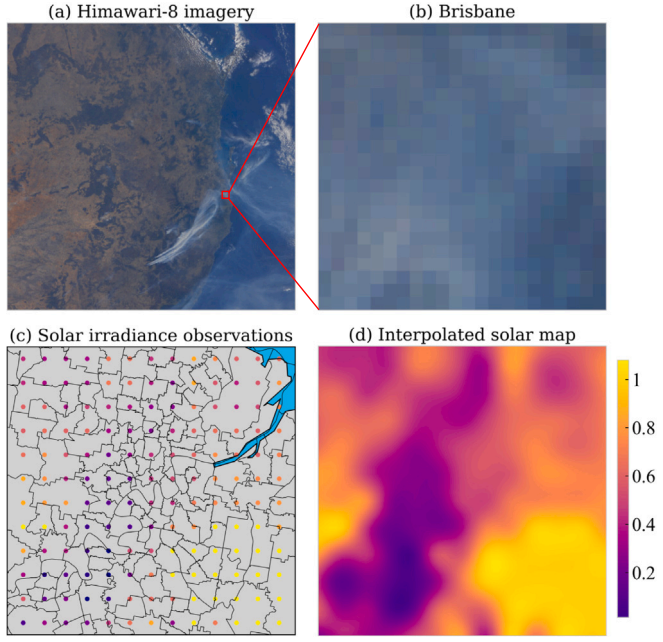

Fig. 4. (a) Himawari-8 satellite imagery of East Australia on December 15, 2019, at 9:30 am (local time); (b) Brisbane. A whiter pixel indicates thicker cloud over the area, associated with a lower CSI value; (c) NSRDB satellite-derived solar irradiance observations; (d) interpolated SIMs (darker color with lower k_t values indicates more shaded areas and vice versa.).

interested region can be represented as:

$$\mathcal{I} = \left\{ \boldsymbol{I}\left(\mathbf{s}_1; t_1\right), \ldots, \boldsymbol{I}\left(\mathbf{s}_n; t_n\right) \right\}^{\top} \tag{2}$$

where n is the number of locations where solar irradiance data is available. When time step t_n at each location are identical, we can decompose $\mathcal{I}$ into:

$$\mathcal{I} = \left\{ \boldsymbol{I}^{(1)}, \boldsymbol{I}^{(2)}, \ldots, \boldsymbol{I}^{(m)} \right\}^{\top} \tag{3}$$

$$\boldsymbol{I}^{(k)} = \left\{ I\left(\mathbf{s}_1; t_k\right), I\left(\mathbf{s}_2; t_k\right), \ldots, I\left(\mathbf{s}_n; t_k\right) \right\} \tag{4}$$

where $k \in \{1, \ldots, m\}$ is temporal index and m is the number of time steps. Then we determine the spatial resolution of interpolated data and create the coordinate meshgrid for mapping the interpolated values to corresponding coordinates.

$$\mathbb{D} = \begin{bmatrix} \mathbf{s}_1 & \cdots & \mathbf{s}_q \\ \vdots & \ddots & \vdots \\ \mathbf{s}_p & \cdots & \mathbf{s}_{pq} \end{bmatrix} = \begin{bmatrix} (x_1, y_1) & \cdots & (x_p, y_p) \\ \vdots & \ddots & \vdots \\ (x_p, y_p) & \cdots & (x_{pq}, y_{pq}) \end{bmatrix}$$

where p and q are the numbers of interpolated latitudes and longitudes, respectively. The total number of interpolated coordinates is equal to $p \times q = R_{obs.}/R_{inter.} \times n$ where $R_{obs.}$ and $R_{inter.}$ respectively denote.

Given the coordinate meshgrid, the estimated value for an unobserved location $\mathbf{s}_0$ can be obtained by calculating the weighted sum of nearby observations as shown below:

$$I^*(\mathbf{s}_0) = \Lambda \times \boldsymbol{I}(\mathbf{s}_i, t_k) = \sum_{i=1}^{n} \lambda_i I(x_i, y_i, t_k) \tag{5}$$

$$\sum_{i=1}^{n} \lambda_i = 1 \tag{6}$$

where $I^*(\mathbf{s}_0)$ is the estimation, x_i and y_i are coordinates at location s_i, and $\Lambda = \{\lambda_1, \ldots, \lambda_n\}$ is the weights vector representing the weights for the n neighbors $\mathbf{s}_n$. Furthermore, by requiring all weights summing up to one in Eq. (6), the estimation is assured unbiased. A single weight can thereby either larger than one or smaller than zero, allowing stronger influence ($\lambda > 1$) or negative influence ($\lambda < 0$) of specific observations.

The theoretical variogram model fitted to the data is used to derive the weights from the spatial covariance structure. To obtain the weights for an unobserved location, a set of equations called the kriging equation system (KES) is formulated [35]. Based on the assumption that the prediction errors is zero and Eq. (6), the final kriging equations can be written as:

$$\begin{cases} \sum_{j=1}^{N} \lambda_j \gamma\left(\mathbf{s}_i - \mathbf{s}_j\right) + \alpha = \gamma\left(\mathbf{s}_i - \mathbf{s}_0\right) \\ \sum_{i=1}^{N} \lambda_i = 1 \end{cases} \tag{7}$$

where α is the Lagrange multiplier for solving the KES. It is possible to obtain the best linear and unbiased estimation by minimizing the estimation variance subject to Eq. (6). Thus, kriging is often referred to as the best linear unbiased estimator (BLUE). Finally, the optimized estimator produces a smooth interpolation as the estimations close to the observations are approaching the observation values very smoothly. An example of interpolated SIM is illustrated in Fig. 4(d).

In this study, SIMs of different spatial resolutions are produced for comparison as shown in Fig. 5. It enables a visual assessment of the effects on the resulting interpolation. Noticeably, the SIMs of spatial resolution higher than 0.5 km are visually identical, while the SIMs of 1 km and 0.5 km resolutions have relatively coarse details and uncealr contours. Therefore, we use a reasonable spatial resolution of 0.2 km for the interpolated SIMs considering both image quality and computational cost of calculation. The forecasting model SIM frames are then saved as images of a fixed dimension of 128 × 128 pixels. Fig. 4 gives an intuitive idea of how satellite data are converted into SIMs.

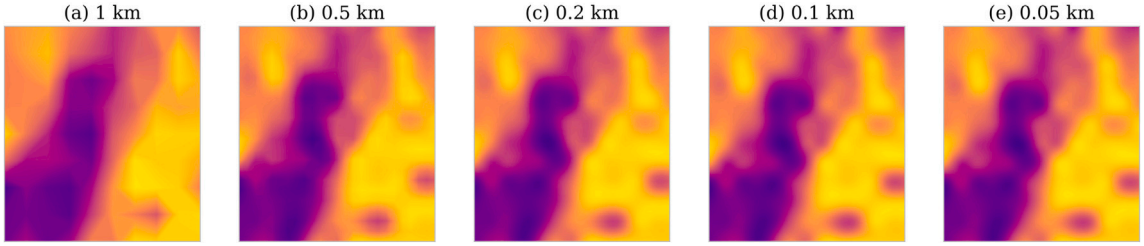

Fig. 5. Effect of spatial resolution on interpolated SIMs.

3.3. Regional forecasts using SIMs

In this stage, a generative adversarial network is trained with the SIM frames. Given an input sequence of SIMs $\boldsymbol{M}_{t-n} = \{M_{t-n}, M_{t-n+1}, \dots, M_t\}$, the prediction process can be formulated as following:

$$\hat{\boldsymbol{M}}_{t+m} = \mathrm{f}(\boldsymbol{M}_{t-n}) \tag{8}$$

where $\hat{\boldsymbol{M}}_{t+m} = \{\hat{M}_{t+1}, \hat{M}_{t+2}, \dots, \hat{M}_{t+m}\} \in \mathbb{R}^{p\times q\times m}$ is a vector of the predicted SIMs and $\mathrm{f}(\cdot)$ is the generative forecasting model. Each value of a pixel on the predicted SIMs value indicates 1-to-m-step ahead CSI prediction at a specific location. The pixel values are further matched with interpolated coordinates at corresponding locations and transformed back to GHI values by multiplying the clear-sky GHI as an inverse process of (1).

3.3.1. Forecasting model

Predicting next-step SIM frame requires an accurate representation of the image evolution in terms of its content and dynamics. Generative adversarial networks (GANs) are unsupervised generative models proposed by [36] and have achieved great success in computer vision tasks such as image generation and video prediction [37]. A typical GANs consists of two models: a generative model (G) and a discriminative model (D) that are both convolutional neural networks (CNNs) as illustrated in Fig. 6. The generator maps random noise signals z to the data space following the distribution $G(z;\Theta_g) \sim P_g$ where Θ_g is generator weights. Thus, it can be trained to predict one or several concatenated frames $Y = \{\mathrm{y}_1, \dots, \mathrm{y}_m\}$ from a sequence of frames $X = \{\mathrm{x}_1, \dots, \mathrm{x}_n\}$ by minimizing distance ℓ_d (e.g., with $d = 1$ or $d = 2$) between the predicted frame and the true frame:

$$\mathcal{L}_d(X,Y) = \ell_d(G(X),Y) = \|(G(X) - Y)\|_d^d \tag{9}$$

In the meanwhile, the discriminator learns to distinguish between the generated and real image by estimating the probability that Y comes from the dataset instead of being produced by the generator $G(X)$.

In this work, a multi-scale version of the generative model proposed for video prediction [38] is used in a transfer learning manner to predict SIMs of the next time step. It is designed to tackle the short-range dependencies issue in convolutions due to the limited size of kennels so that it learns internal representations at various scales. The multi-scale generative model takes four different sizes of images as inputs. The prediction at a lower scale is used as an input for the network at a higher scale. We define u_k to be the upscaling operator towards size s_k (i.e., $s_1 = 4\times4$, $s_2 = 8\times8$, $s_3 = 16\times16$ and $s_4 = 32\times32$). The prediction of size s_k can be obtained by recursively predicting from lower size s_{k-1} in a concatenated way, which is written by:

$$\hat{Y}_k = G_k(X) = u_k(\hat{Y}_{k-1}) + G'_k\left(X_k, u_k(\hat{Y}_{k-1})\right) \tag{10}$$

where X_k and Y_k denote the downscaled frames of size s_k and G'_k is a network that predicts a course frame of $Y_k - u_k(Y_{k-1})$ by learning from X_k. The architecture of the multi-scale model is shown in Fig. 6 and Table 1.

3.3.2. Adversarial training

The objective of adversarial training is to train a discriminator D that correctly classifies the predicted images and real images from the dataset as stated in the previous section. The discriminator is also a multi-scale convolutional network and takes a sequence of frames where only the last frame can be either real or generated by G and the rest of the frames are always from the dataset. This allows the discriminator to make use of temporal information and the generator to produce SIMs that are temporally correlated to the input sequence. To simplify the training process, the output of the discriminator is simply expressed in two classes:

$$\begin{cases} 0 = D(G(X)) \\ 1 = D(Y) \end{cases} \tag{11}$$

After specifying the training goal, we can respectively optimize generator weights Θ_g and discriminator weights Θ_d by performing Stochastic Gradient Descent (SGD) minimization with the following loss functions. The adversarial loss function we use to train D is:

$$\begin{aligned}\mathcal{L}_{adv}^{D}(X,Y) = \sum_{k=1}^{N_{\text{scale}}} &\ell_{bce}\left(D_k(X_k, Y_k), 1\right) \\ &+ \ell_{bce}\left(D_k(X_k, G_k(X)), 0\right)\end{aligned} \tag{12}$$

where N_{scale} is the total number of image scales and ℓ_{bce} is the binary cross-entropy loss which is defined as:

$$\ell_{bce}(Y,\hat{Y}) = -\sum_i \hat{Y}_i \log\left(Y_i\right) + \left(1-\hat{Y}_i\right)\log\left(1-Y_i\right) \tag{13}$$

where $Y_i \subset \{0,1\}$ and $\hat{Y}_i \in [0,1]$. During the training of D, the weights of G is keeping fixed. Similarly, while keeping Θ_d fixed, we can learn Θ_g from input sample (X,Y) by minimizing the adversarial loss:

$$\mathcal{L}_{adv}^{G}(X,Y) = \sum_{k=1}^{N_{\text{scales}}} L_{bce}\left(D_k\left(X_k, G_k\left(X_k\right)\right), 1\right) \tag{14}$$

However, minimizing this loss alone makes the generated frames $\hat{Y}$ can deceive D as much as possible but can be dissimilar to real images Y. To alleviate this issue, penalization on distance ℓ_d is introduced as an additional constraint to improve similarity by using $\mathcal{L}_d$ loss. In [38], the authors proposed a new loss function called Gradient Difference Loss (GDL), which directly penalizes gradient differences between the prediction and the ground truth by considering neighboring pixel intensity on each image, which is defined as:

$$\begin{aligned}\mathcal{L}_{gdl}(\hat{Y},Y) = \sum_{i,j} &\left|\left|\mathrm{y}_{i,j} - \mathrm{y}_{i-1,j}\right| - \left|\hat{\mathrm{y}}_{i,j} - \hat{\mathrm{y}}_{i-1,j}\right|\right|^{\alpha} \\ &+ \left|\left|\mathrm{y}_{i,j-1} - \mathrm{y}_{i,j}\right| - \left|\hat{\mathrm{y}}_{i,j-1} - \hat{\mathrm{y}}_{i,j}\right|\right|^{\alpha}\end{aligned} \tag{15}$$

where $\alpha \geq 1$ and $|\cdot|$ is absolute function. Therefore, the final loss used to train the generator is a combined loss composed of the previous losses (9), (14), and (15):

$$\mathcal{L}(X,Y) = \phi_{\text{adv}}\mathcal{L}_{adv}^{G}(X,Y) + \phi_{\ell_p}\mathcal{L}_p(X,Y) + \phi_{gdl}\mathcal{L}_{gdl}(X,Y) \tag{16}$$

with parameters $\phi_{adv} = 0.05$, $\phi_{\ell_p} = 1$, and $\phi_{gdl} = 1$ according to [38]. The first and third terms of (16) on the right side enhance the sharpness

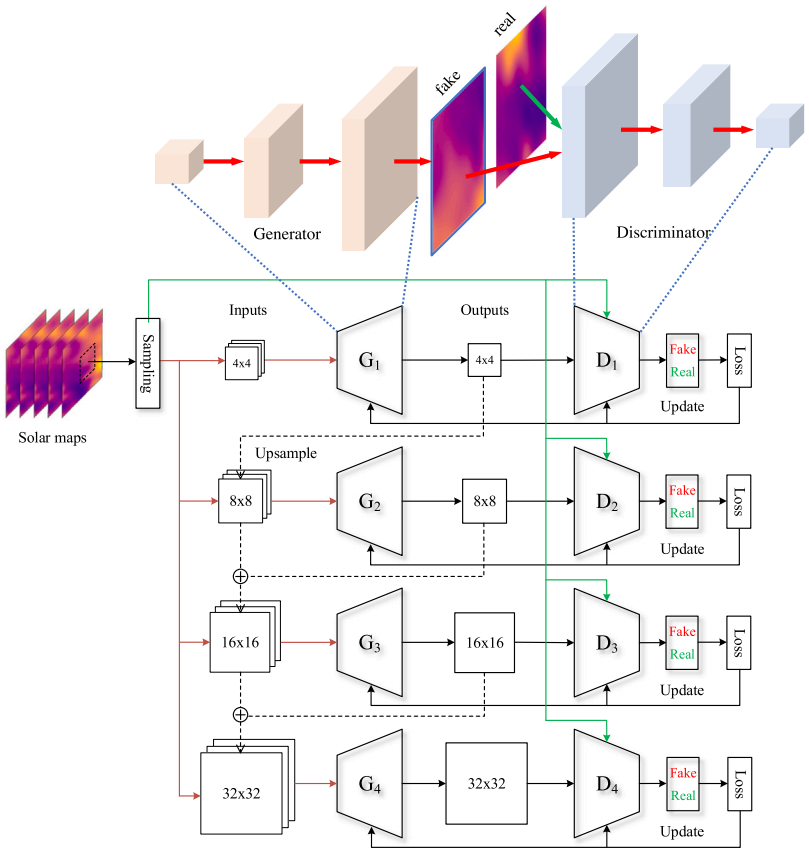

Fig. 6. Architecture of multi-scale GAN.

Table 1
The multi-scale generative adversarial model architecture.

Generator	G_1	G_2	G_3	G_4
No. of feature maps	(128, 256, 128)	(128, 256, 128)	(128, 256, 512, 256, 128)	(128, 256, 512, 256, 128)
Conv. kernel size	(3, 3, 3, 3)	(5, 3, 3, 5)	(5, 3, 3, 3, 5)	(7, 5, 5, 5, 5, 7)
Discriminator	D_1	D_2	D_3	D_4
No. of feature maps	(64)	(64, 128, 128)	(128, 256, 256)	(128, 256, 512, 128)
Conv. kernel size	(3)	(3, 3, 3)	(5, 5, 5)	(7, 7, 5, 5)
FC layer size	(512,256)	(1024,512)	(1024,512)	(1024,512)

of predicted images and the second term increases the similarity to the ground truth.

Since we take advantage of the transfer learning technique, we use a pre-trained multi-scale generative network and fine-tune it on our own datasets of randomly cropped 32 × 32 patches of input image sequences. To ensure most patches show enough movement, we remove the SIMs under clear and overcast conditions that are visually consistent over time, but the dataset size can be still greatly augmented by cropping the frames such that we have sufficient data to avoid over-fitting. The reason for using 32 × 32 patches is that larger size will lead to the out-of-memory issue because the output size of the fully-connected (FC) layers of the discriminator depends on the input image size and can blow up very quickly. For example, for an input image size of 64 × 64, going from 128 feature maps to an FC layer with 512 nodes, we need a connection with $64 * 64 * 128 * 512 = 268,435,456$ weights. However, we only need the discriminator for training, and the generator network is fully convolutional, so we can test the weights over images of any size. We set the learning rate ρ_D to 0.02 to train the discriminator, and set ρ_G start at 0.04 and is reduced to 0.005 over time to train the generator.

3.4. Irradiance-to-power conversion

Finally, the predicted SIMs are used for PV power estimation. To this end, the values on the predicted SIMs are assigned with corresponding geographical coordinates such that the predictions at any locations can be retrieved from the map. Then the extracted CSI values are transformed back to GHI values by multiplying the clear-sky GHI as a inverse process in Eq. (1):

$$GHI_{\text{prediction}} = CSI_{\text{prediction}} \times GHI_{\text{clear-sky}} \tag{17}$$

For validation, PV power predictions are required. As the output of the above model is solar irradiance, the GHI forecasts should be further converted to PV power data with a irradiance-to-power conversion model. A direct conversion from irradiance to power can be found in [39], which considers PV system size and ratio of PV nominal power to the standard irradiance.

$$P(s) = \frac{K}{(\sqrt{s}/(2\pi \cdot 0.02))s + 1} \cdot G(s) \tag{18}$$

where $P(s)$ and $G(s)$ respectively denote the PV power and GHI data in the frequency domain, K is the ratio of PV nominal power to the standard irradiance of 1000 W/m^2, and S is PV system area. Eq. (18)

Table 2
Irradiance-to-power model parameters.

Parameters	System capacity	AC/DC ratio	Tilt angle	Azimuth angle	Inverter efficiency	System loss	Array type
Values	*	1.1	25°	26°	96%	10.1%	Fixed

indicates that the variability becomes inversely proportional to the square root of PV system area.

In this case, the PV systems are distributed systems of small areas. They are more vulnerable to small irradiance change than large-scale PV systems. Besides, due to the geographic dispersion in practical PV systems, the diversity in irradiance variability can be greatly relieved in PV power profiles. Thus, this model could result in larger errors for the distributed PV systems.

To make more accurate forecasts, we use National Renewable Energy Laboratory's System Advisor Model (SAM) accounting for various parameters. It is implemented by using PySAM, a Python interface for the models found in SAM simulation core. Due to the lack of system specifications, we use fixed values for AC/DC ratio, tile angle, inverter efficiency, system loss, and array type by considering both simplicity and availability. For the azimuth angle, we assume that the PV systems are oriented at a tilt angle that is equal to the location's latitude for the maximum possible energy generation. According to a study conducted by the University of Queensland, the ideal value for rooftop solar panels in Brisbane is 26°, facing North. These approximation only affects the total amount of PV power yield, but has little impact on how PV power output changes as it is dominated by the solar irradiance variation. The specific model parameters are shown in Table 2.

4. Experiments

To fully validate the effectiveness of the proposed method, we carry out three experiments on SIMs prediction, solar irradiance forecasting, and PV out estimation. First, we use the generative model to forecast regional solar irradiance by producing SIMs from a sequence of chronological frames. Then, we evaluate the forecasting performance by comparing the predicted SIMs with the predictions from other benchmarks at observed locations. Finally, we verify the effect of our method by estimating the output of 30 BTM PV systems at unobserved locations.

4.1. Prediction of SIMs

In this section, we predict the next-step SIMs by using the multi-scale generative model with a sequence of five input frames. We compare the results with the frames generated without using adversarial training and the last frame of the input sequence. The idea of using the copy of the last input is equivalent to the persistent model, but for the entire region of interest. The non-adversarial model can be regarded as a fully convolutional network of the aim to investigate the contribution of the adversarial loss in SIM prediction tasks.

To evaluate the quality of the predicted SIMs, we first compute the Peak Signal to Noise Ratio (PSNR) between the true frame Y and the prediction $\hat{Y}$:

$$\mathrm{PSNR}(Y,\hat{Y}) = 10\log_{10}\frac{\max_{\hat{Y}}^2}{\frac{1}{N}\sum_{i=0}^{N}\left(Y_i-\hat{Y}_i\right)^2} \tag{19}$$

where $\max_{\hat{Y}}$ is the maximum possible pixel value of the image and equals to 1 since the images are normalized. A larger PSNR score indicates a greater similarity between two frames.

Besides, we measure the sharpness difference (SD) between Y and the prediction $\hat{Y}$ based on the difference of gradients between two images, which is a commonly applied evaluation method for image generation and is defined as:

$$\mathrm{SD} = 10\log_{10}\frac{\max_{\hat{Y}}^2}{\frac{1}{N}\left(\sum_i\sum_j\left|\left(\nabla_i Y+\nabla_j Y\right)-\left(\nabla_i\hat{Y}+\nabla_j\hat{Y}\right)\right|\right)} \tag{20}$$

where $\nabla_i Y = \left|Y_{i,j}-Y_{i-1,j}\right|$ and $\nabla_j Y = \left|Y_{i,j}-Y_{i,j-1}\right|$. A larger sharpness difference means better quality of the prediction.

Table 3
Comparison of the accuracy of the predicted SIMs on the test set.

	PSNR	SD
Adversarial	**18.6**	0.81
Non-adversarial	16.3	0.67
Last input	17.9	**0.86**

The quantitative measures on the test set are given in Table 3. The results indicate that the adversarial model outperforms the non-adversarial model in terms of both PSNR and SD, and achieves the highest PSNR score of 18.6. However, its SD score is slightly lower than that of the copy of the last frame in the input sequence because the sharpness of the adversarial predictions is deteriorated by introducing the ℓ_1 norm that uses median values of individual pixel predictions.

Fig. 7 demonstrates the predicted SIMs of both adversarial and non-adversarial models on four different days. We note that the prediction of the adversarial model is more visually similar to the ground truth in the moving areas. As expected, the image similarity score is higher, but the sharpness score is a little lower than the last input frame due to the deteriorated contours of moving areas. In contrast, the non-adversarial results appear more static and blurred due to the lack of an adversarial training process, which results in further deteriorated PSNR and SD scores.

4.2. Solar irradiance forecasting at observed locations

In this section, we compare the effectiveness of our forecasting method at observed locations, meaning that the historical solar irradiance data from 10 random locations out of all data points (red dots in Fig. 2) are used for validation. In addition to the results of the adversarial and non-adversarial models, we also introduce two statistic models, namely least absolute shrinkage and selection operator (Lasso), Extreme Gradient Boosting (XGBoost), and a machine learning model-long short-term memory (LSTM) as the benchmark models. They are exclusively trained and validated on the same data at the selected 10 locations. The Lasso and XGBoost models are available in a *scikit-learn* machine learning library in Python and can be easily trained with a small amount of data to achieve accurate forecasts.

To evaluate forecasting performance, we use the smart persistence model as a baseline reference model. It is based on the assumption that the future irradiance will remain unchanged over the next forecast horizon and achieve high accuracy in low-variation periods of irradiance. The prediction of smart persistence is simply equal to:

$$\hat{y}_{t+\tau} = k_t^{(\mathrm{cs})}\cdot I_{t+\tau}^{(\mathrm{cs})} \tag{21}$$

where $k_t^{(\mathrm{cs})}$ is CSI, $I_{t+\tau}^{(\mathrm{cs})}$ is clear-sky irradiance at next horizon $t+\tau$.

We consider three commonly used error metrics in this work to evaluate solar irradiance and PV power predictions, namely, normalized mean absolute error (nMAE), normalized mean bias error (nMBE), and normalized root mean square error (nRMSE). They are given by:

$$\mathrm{nMAE} = \frac{1}{n}\sum_{t=1}^{n}|y_t-\hat{y}_t|/\bar{y} \tag{22}$$

$$\mathrm{nMBE} = \frac{1}{n}\sum_{t=1}^{n}(y_t-\hat{y}_t)/\bar{y} \tag{23}$$

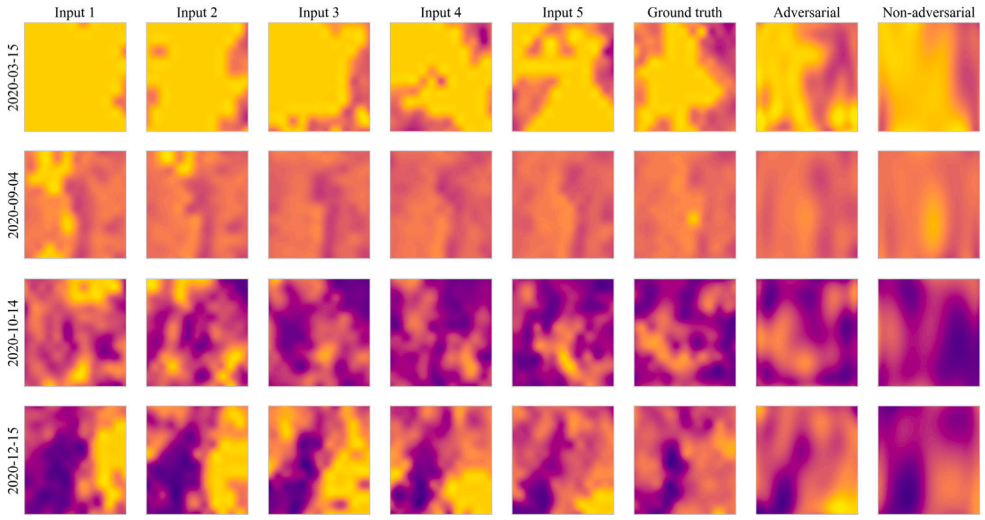

Fig. 7. Predictions of SIMs generated by the adversarial and non-adversarial models on different days.

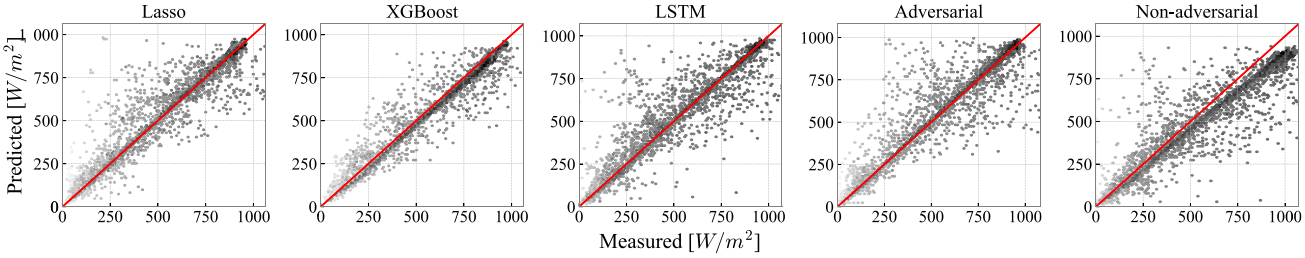

Fig. 8. Scatter plot of the predictions produced by different forecasting models. The results show the average values of the 10 selected observed points.

Table 4
Solar irradiance forecasting results of different models at 10 observed points on the test set.

	nMAE [%]	nMBE [%]	nRMSE [%]	FS [%]
Smart Pers.	14.2 ± 0.5	0.1 ± 0.0	26.4 ± 1.2	0.0
Lasso	12.3 ± 0.3	0.2 ± 0.1	23.5 ± 0.5	11.8 ± 2.5
XGBoost	12.1 ± 0.2	−1.2 ± 0.1	22.9 ± 0.2	13.3 ± 2.8
LSTM	13.3 ± 1.5	1.2 ± 0.8	24.2 ± 1.5	8.3 ± 3.8
Adversarial	13.8 ± 1.3	0.3 ± 0.9	24.5 ± 1.1	7.2 ± 3.2
Non-adversarial	19.5 ± 3.2	−12.4 ± 1.6	35.2 ± 3.4	−33.2 ± 10.3

$$\text{nRMSE} = \sqrt{\frac{1}{n}\sum_{t=1}^{n}(y_t - \hat{y}_t)^2}/\bar{y} \tag{24}$$

where n is the number of predictions, y_t, $\hat{y}_t$, and $\bar{y}$ are measured, predicted and mean values at time t, respectively.

Besides, forecast skill (SF) is used to measure the improvement of a forecasting model over the reference model:

$$\text{skill} = 1 - \frac{\text{nRMSE}}{\text{nRMSE}_\text{p}} \tag{25}$$

where nRMSE_p is the nRMSE of the smart persistence.

The forecasting results shown in Table 4, which are represented as "mean±standard deviation" for all 10 locations. It can be seen in general, the statistic models Lasso and XGBoost outperform the others by achieving high forecast skills of 11.8 ± 2.5% and 13.3 ± 2.8% and having lower nMAE, nMBE, and nRMSE values. The forecast skill of LSTM is 8.3 ± 3.8%, which is lower than that of the statistic models. This is probably because LSTM requires more training data than the Lasso and XGBoost and the training process is more complex. Regarding the GAN, it has a comparable forecasting accuracy with LSTM with a forecast skill of 7.2 ± 3.2% as well as other metrics. However, it shows lower standard deviations than LSTM, which indicates more stable performance at all the selected locations. As for the model without adversarial training, the model is equivalent to a feed-forward fully-connected network. It is found that its forecasting performance is greatly reduced due to the lower similarity and sharpness of the predicted SIMs.

Fig. 8 compares the forecasting results generated by different forecasting models. Each subplot shows the average values for the 10 selected observed points. The red line means the predictions are equal to the measurements. It is observed that the predictions of Lasso and XGBoost are more concentrated with few outliers, whereas the LSTM and GAN have more predictions that are far from the equal line, which indicates larger forecasting errors and deteriorated accuracy. As for the non-adversarial model, it shows an obvious bias below the equal line meaning that the predictions are generally lower than the true values and produce a low nMBE of −10.4 ± 1.6%. Fig. 9 demonstrates the predicted solar variation of different forecasting models on 22 December 2020 at an observed point.

4.3. PV power forecasting at unobserved locations

In this section, we evaluate the forecasting framework by estimating power generations of distributed PV systems at unobserved locations. We select 30 rooftop PV systems in the target region for validation purposes and assume that the historical PV output data is only available to the owners due to privacy and security concerns. As a result, these PV systems are operating behind-the-meter and their power generations are not monitored by the utilities.

One possible solution is to utilize observed data to infer the behaviors of the neighboring PV systems since they are spatio-temporally correlated and the outputs are likely to have similar patterns as plotted in Fig. 10. The relationship between the neighboring systems $p_x^{(i)}$ and

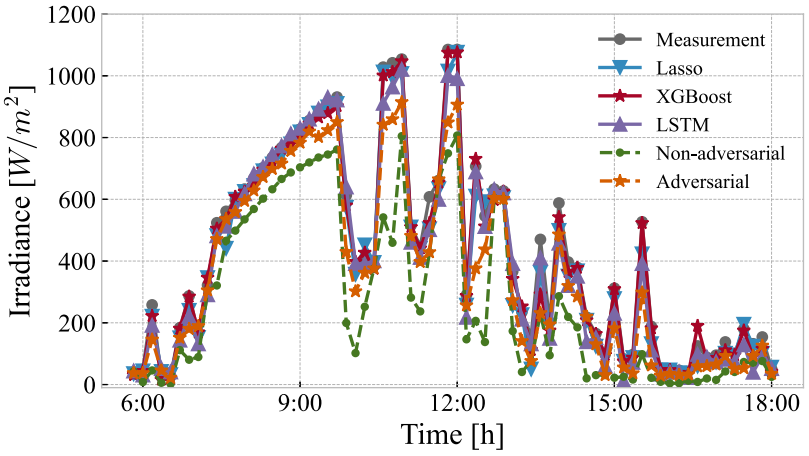

Fig. 9. Predictions of solar irradiance of different forecasting methods at an observed points on 22 December, 2020.

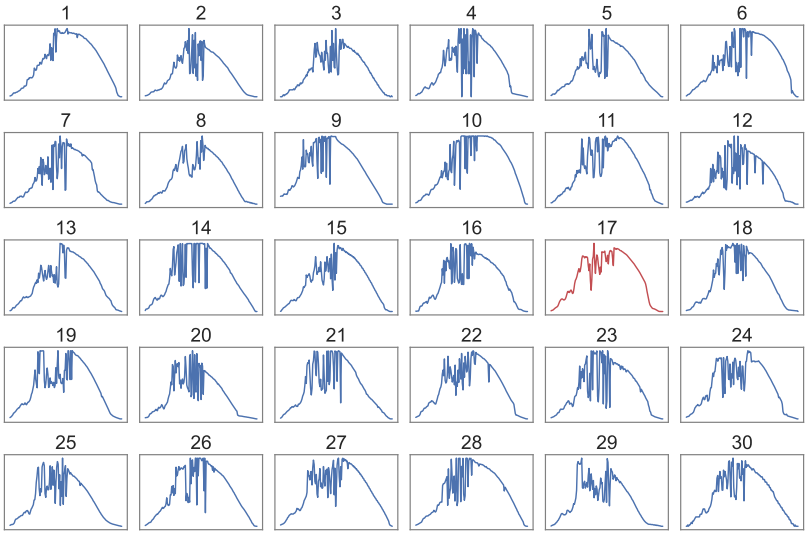

Fig. 10. Normalized power output curves of the 30 selected PV systems at unobserved locations 1st December, 2020. The red curve has the highest correlation with the others and is used as a reference for estimation.

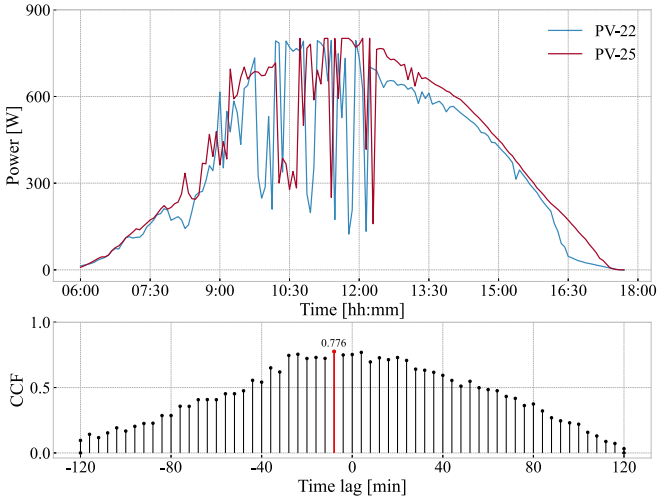

Fig. 11. The time lag between PV-22 and PV-25 on 2020 December 1. The PV output time series are shown in the top figure and the cross-correlation function (CCF) is shown below.

$p_y^{(i)}$ can be measured by correlation coefficients. As an example, Fig. 11 shows the cross correlation between two PV systems PV-22 and PV-25 (about 3.42 km apart) on 2020 December 1. A maximum correlation of 0.776 is observed at a time lag +20 min. This indicates that the PV power variation at PV-22 might cause similar variations at PV-25 20 min later on that day. Therefore, we compute the Pearson Correlation Coefficient (PCC) for all PV systems pairs to find the maximum correlation coefficient, which is defined as follows:

$$\gamma = \frac{\sum(p_x^{(i)} - \bar{p}_x)(p_y^{(i)} - \bar{p}_y)}{\sqrt{\sum(p_x^{(i)} - \bar{p}_x)^2 (p_y^{(i)} - \bar{p}_y)^2}} \tag{26}$$

Fig. 12 illustrates the calculated PCCs for each PV site. It is seen that most systems are correlated to each other, but some of them have low correlation due to a variety of reasons such as different panel specifications, shading, and even dust accumulation. For example, PV-30 is geographically close to PV-27, but they have a lower PCC of 0.87 compared to that of 0.9 between PV-30 and PV-18 even though they show a longer distance. In this study, we choose PV-17 to be observed as a best-case reference system since it has the highest PCC of 0.873. A higher correlation indicates a higher possibility of similarity. As a result, we can simply estimate PV outputs at other locations based on the approximation that they have the same patterns as PV-17 (denoted as a shift method).

Table 5
The PV power forecasting results by different forecasting models.

Site	Metric [%]	Pers.	Lasso	XGBoost	LSTM	Shift	GAN
PV-1	nMAE	12.34	11.42	**11.23**	12.513	15.69	11.74
	nMBE	0.0	0.35	**−0.12**	−0.65	−12.42	0.55
	nRMSE	24.21	22.92	23.17	23.84	27.32	**22.64**
	Skill	–	5.33	4.30	1.53	−12.85	**6.48**
PV-3	nMAE	14.23	**12.59**	12.72	13.89	17.83	12.85
	nMBE	0.0	**0.21**	−0.35	−3.25	5.29	2.41
	nRMSE	28.32	27.41	27.29	28.70	31.04	**25.75**
	Skill	–	3.21	3.64	−1.34	−9.60	**9.04**
PV-5	nMAE	11.79	10.95	**10.82**	11.13	14.43	11.34
	nMBE	0.0	**0.32**	−0.65	−2.34	−6.42	2.26
	nRMSE	25.94	25.41	24.89	26.31	28.74	**24.28**
	Skill	–	2.04	4.05	−3.77	−10.79	**6.40**
PV-7	nMAE	12.87	11.16	**11.05**	12.53	15.43	13.29
	nMBE	0.0	0.43	**−0.31**	−1.21	−10.20	−0.89
	nRMSE	25.32	24.93	24.57	24.89	27.94	**24.12**
	Skill	–	1.54	2.96	1.70	−10.35	**4.74**
PV-9	nMAE	12.76	12.02	**11.75**	11.93	14.84	12.42
	nMBE	0.0	**0.24**	−0.52	−2.74	−6.13	2.43
	nRMSE	26.23	24.48	24.67	27.53	29.31	**23.88**
	Skill	–	6.67	5.96	−4.96	−11.74	**8.96**
PV-2	nMAE	11.95	11.03	10.95	13.80	16.23	12.03
	nMBE	0.0	**0.28**	0.15	−2.38	−5.31	1.49
	nRMSE	25.59	23.10	23.42	24.56	27.35	**22.87**
	Skill	–	9.73	8.48	4.03	−6.88	**10.63**
PV-4	nMAE	13.56	12.21	**12.04**	11.94	15.31	12.74
	nMBE	0.0	**0.53**	−0.97	−1.04	−6.92	1.53
	nRMSE	26.94	25.83	25.54	26.12	27.71	**24.66**
	Skill	–	4.12	5.20	1.56	−2.86	**8.52**
PV-6	nMAE	11.43	10.72	**10.28**	10.93	14.21	11.03
	nMBE	0.0	**0.05**	0.59	1.42	−3.42	1.48
	nRMSE	25.22	23.89	23.62	26.17	27.12	**22.37**
	Skill	–	5.24	6.34	4.52	−7.53	**11.31**
PV-8	nMAE	12.24	11.39	**10.94**	12.84	16.21	11.85
	nMBE	0.0	**0.14**	−0.23	−1.47	3.39	1.32
	nRMSE	25.85	25.46	24.98	26.32	29.17	**24.21**
	Skill	–	.51	3.37	−1.82	−12.84	**6.34**
PV-10	nMAE	13.74	13.49	**13.04**	13.42	15.31	12.98
	nMBE	0.0	**0.67**	0.94	−3.92	−9.28	1.89
	nRMSE	27.35	26.92	**26.39**	28.42	31.17	26.47
	Skill	–	1.57	**3.51**	−3.91	−13.97	3.22

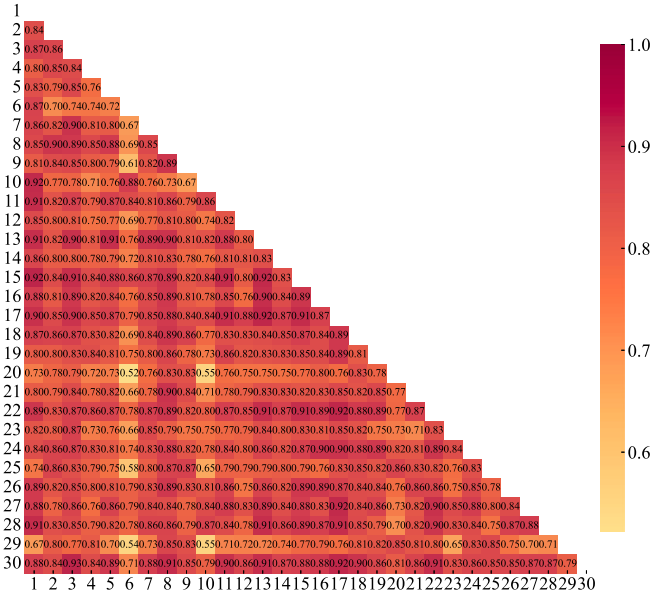

Fig. 12. Correlation matrix of PV outputs.

Table 6
PV power forecasting results at unobserved locations.

	nMAE [%]	nMBE [%]	nRMSE [%]	FS [%]
Pers.	11.61 ± 0.58	0.0 ± 0.0	22.97 ± 1.45	0.0
Lasso	10.83 ± 1.34	0.89 ± 0.33	22.21 ± 0.63	3.31 ± 1.61
XGBoost	10.68 ± 1.26	0.81 ± 0.31	22.14 ± 0.51	3.62 ± 1.52
LSTM	12.19 ± 1.22	−0.42 ± 1.13	24.31 ± 1.56	−3.87 ± 2.81
Shift	15.72 ± 2.91	3.71 ± 1.68	25.38 ± 2.42	−10.49 ± 5.42
Adversarial	10.87 ± 0.92	1.54 ± 1.26	20.46 ± 0.75	10.93 ± 2.35

In contrast, forecasting for individual PV systems is relatively straightforward because it can be achieved by training any time-series forecasting models on the user's historical power generation. Therefore, we use the previous models (i.e., Lasso, XGBoost, and LSTM) for benchmarking based on the assumption that the models are trained by the PV system owners. The non-adversarial model is not used in this case since it has the worst performance.

Table 5 shows the PV power forecasting results of each individual PV system. Due to page limit, we only include the results of 10 PV systems for better illustration. Table 6 summarizes the PV power forecasting results of all PV systems in a form of "mean±std". The statistical models generally show comparable accuracy with forecast skill of 3.31 ± 1.61 and 3.62 ± 1.52. However, the LSTM and shift method give unsatisfactory results which are worse than the simple persistence model, especially for large ramp events. On the contrary, the proposed approach outperforms the others showing minimal forecasting errors and the highest forecast skill of 10.93 ± 2.35. Fig. 13 shows nMAE, nMBE, nRMSE, and forecast skill of different methods in a box plot at 30 PV sites. The values of each error for a PV system are scatter-plotted for better visualization. It is found that the proposed method can predict PV power output at unobserved locations with the highest accuracy.

5. Conclusion

This paper is mainly concerned with producing regional forecasts of solar irradiance, as might be required by those studies for solar energy assessment in high-penetration areas. In this article, we proposed a generative approach to forecast solar irradiance variation of an entire region by generating SIMs with a multi-scale generative adversarial network (GAN). Moreover, we introduce SIMs for solar forecasting for the first time, which allow for the forecasts of solar irradiance in a flexible geographical and give an intuitive view of how solar irradiance varies over time. Through case studies against benchmarks and commonly used models for solar forecasting, the superiority of the proposed approach can be confirmed. More specifically, this method achieves competing forecasting accuracy at single locations, while considering regional-level solar irradiance variation of the interested area. Besides, the proposed method outperforms the benchmarks in estimating outputs of the BTM PV systems with the highest forecast skill of $10.93 \pm 2.35\%$ at unobserved locations. Thus, it can be deemed useful when assessing solar resources, making decisions of power system control, and designing electricity market.

The main challenge preventing this approach from practical deployment is the unavailability of real-time satellite data. Even thought the data is available, the knowledge gap of transforming the satellite data to ground solar irradiance still exists. In this study, we only consider one-step ahead forecasts as the forecast horizon is limited by the temporal resolution of input data. However, long-sequence predictions are preferred in the applications such as PV ramp-rate control for better performance. In future work, we will continue to explore regional solar forecasting methods with using state-of-the-art models and various data sources, consider multiple forecast horizons with finer temporal resolution, and potentially integrate it to real-world applications.

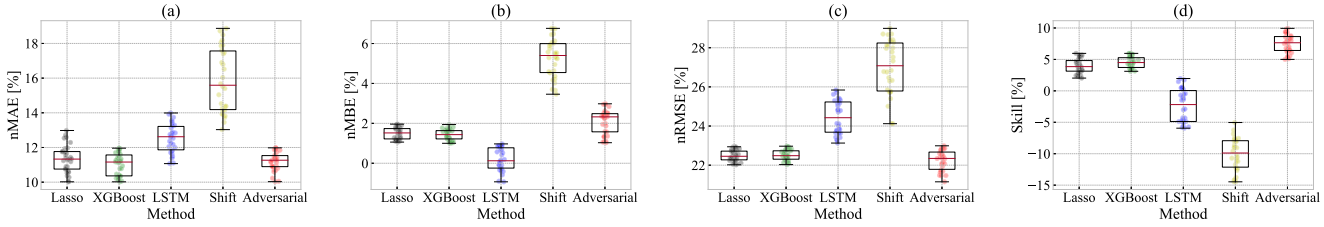

Fig. 13. Box plot of PV power forecasting errors of different methods at the 30 unobserved locations: (a) nMAE, (b) nMBE, (c) nRMSE, and (d) Skill. The individual forecasting errors of each model are plotted with different colors.

CRediT authorship contribution statement

Haoran Wen: Conceptualization, Software, Visualization, Writing – original draft, Writing – review & editing. **Yang Du:** Methodology, Investigation, Supervision, Writing – review & editing. **Xiaoyang Chen:** Methodology. **Eng Gee Lim:** Project administration, Resource, Investigation. **Huiqing Wen:** Supervision, Writing – review & editing. **Ke Yan:** Validation.

Declaration of competing interest

The authors declare that they have no known competing financial interests or personal relationships that could have appeared to influence the work reported in this paper.

Acknowledgments

AI University Research Centre (AI-URC), China through XJTLU Key Programme Special Fund (KSF-P-02) and research development fund of XJTLU), China (RDF-17-01-28).

References

[1] C. Breyer, D. Bogdanov, A. Gulagi, A. Aghahosseini, L.S. Barbosa, O. Koskinen, M. Barasa, U. Caldera, S. Afanasyeva, M. Child, et al., On the role of solar photovoltaics in global energy transition scenarios, Prog. Photovolt., Res. Appl. 25 (8) (2017) 727–745.
[2] M. Diagne, M. David, P. Lauret, J. Boland, N. Schmutz, Review of solar irradiance forecasting methods and a proposition for small-scale insular grids, Renew. Sustain. Energy Rev. 27 (2013) 65–76.
[3] S. Maharjan, D.S. Kumar, A.M. Khambadkone, Enhancing the voltage stability of distribution network during PV ramping conditions with variable speed drive loads, Appl. Energy 264 (2020) 114733.
[4] N. Haghdadi, A. Bruce, I. MacGill, R. Passey, Impact of distributed photovoltaic systems on zone substation peak demand, IEEE Trans. Sustain. Energy 9 (2) (2017) 621–629.
[5] B.C. Erdener, C. Feng, K. Doubleday, A. Florita, B.-M. Hodge, A review of behind-the-meter solar forecasting, Renew. Sustain. Energy Rev. 160 (2022) 112224.
[6] T. Stoffel, A. Andreas, NREL Solar Radiation Research Laboratory (srrl): Baseline Measurement System (bms); Golden, Colorado (data), Tech. Rep., National Renewable Energy Lab.(NREL), Golden, CO (United States), 1981.
[7] L. Bird, M. Milligan, D. Lew, Integrating Variable Renewable Energy: Challenges and Solutions, Tech. Rep. NREL/TP-6A20-60451, National Renewable Energy Laboratory (NREL), Golden, CO, USA, 2013.
[8] J.G. da Silva Fonseca Junior, T. Oozeki, H. Ohtake, T. Takashima, K. Ogimoto, Regional forecasts of photovoltaic power generation according to different data availability scenarios: a study of four methods, Prog. Photovolt., Res. Appl. 23 (2015) 1203–1218.
[9] T. Hoff, Behind-the-meter (BTM) PV forecast integration with load forecasting, in: Utility Variable Generation Integration Group Forecasting Workshop, 2016.
[10] J. Kleissl, Current state of the art in solar forecasting, 2010.
[11] X. Zhang, Y. Li, S. Lu, H.F. Hamann, B.-M.S. Hodge, B. Lehman, A solar time based analog ensemble method for regional solar power forecasting, IEEE Trans. Sustain. Energy 10 (2019) 268–279.
[12] S. Killinger, D. Lingfors, Y.-M. Saint-Drenan, P. Moraitis, W.G. van Sark, J. Taylor, N.A. Engerer, J.M. Bright, On the search for representative characteristics of PV systems: Data collection and analysis of PV system azimuth, tilt, capacity, yield and shading, Sol. Energy (2018).
[13] E. Lorenz, T. Scheidsteger, J. Hurka, D. Heinemann, C. Kurz, Regional PV power prediction for improved grid integration, Prog. Photovolt., Res. Appl. 19 (2011).
[14] Y.-M. Saint-Drenan, G. Good, M. Braun, A probabilistic approach to the estimation of regional photovoltaic power production, Sol. Energy 147 (2017) 257–276.
[15] Y.-M. Saint-Drenan, S. Vogt, S. Killinger, J.M. Bright, R. Fritz, R.W.E. Potthast, Bayesian parameterisation of a regional photovoltaic model – Application to forecasting, Sol. Energy (2019).
[16] H.R. Shaker, D. Manfre, H. Zareipour, Forecasting the aggregated output of a large fleet of small behind-the-meter solar photovoltaic sites, Renew. Energy 147 (2020) 1861–1869.
[17] A. Alcántara, I.M. Galván, R. Aler, Deep neural networks for the quantile estimation of regional renewable energy production, Appl. Intell. (2022).
[18] G. Reikard, Predicting solar radiation at high resolutions: A comparison of time series forecasts, Sol. Energy 83 (2009) 342–349.
[19] E. Lorenz, J. Hurka, D. Heinemann, H.-G. Beyer, Irradiance forecasting for the power prediction of grid-connected photovoltaic systems, IEEE J. Sel. Top. Appl. Earth Obs. Remote Sens. 2 (2009) 2–10.
[20] A. Gastli, Y. Charabi, Solar electricity prospects in oman using GIS-based solar radiation maps, Renew. Sustain. Energy Rev. 14 (2) (2010) 790–797.
[21] J. de Hoog, M. Perera, K. Bandara, D. Senanayake, S. Halgamuge, Solar PV maps for estimation and forecasting of distributed solar generation, in: ICML 2021 Workshop on Tackling Climate Change with Machine Learning, 2021.
[22] F. Wang, Z. Zhang, C. Liu, Y. Yu, S. Pang, N. Duić, M. Shafie-Khah, J.P. Catalao, Generative adversarial networks and convolutional neural networks based weather classification model for day ahead short-term photovoltaic power forecasting, Energy Convers. Manage. 181 (2019) 443–462.
[23] M. Khodayar, S. Mohammadi, M.E. Khodayar, J. Wang, G. Liu, Convolutional graph autoencoder: A generative deep neural network for probabilistic spatio-temporal solar irradiance forecasting, IEEE Trans. Sustain. Energy 11 (2) (2019) 571–583.
[24] A. Debnath, G. Waghmare, H. Wadhwa, S. Asthana, A. Arora, Exploring generative data augmentation in multivariate time series forecasting: opportunities and challenges, Solar-Energy 137 (2021) 52–560.
[25] C. Jiang, Y. Chen, Y. Mao, Y. Chai, M. Yu, Forecasting spatio-temporal renewable scenarios: a deep generative approach, 2019, arXiv preprint arXiv:1903.05274.
[26] X. Huang, Q. Li, Y. Tai, Z. Chen, J. Liu, J. Shi, W. Liu, Time series forecasting for hourly photovoltaic power using conditional generative adversarial network and Bi-LSTM, Energy 246 (2022) 123403.
[27] F. Li, H. Zheng, X. Li, A novel hybrid model for multi-step ahead photovoltaic power prediction based on conditional time series generative adversarial networks, Renew. Energy 199 (2022) 560–586.
[28] F. Meng, Q. Zou, Z. Zhang, B. Wang, H. Ma, H.M. Abdullah, A. Almalaq, M.A. Mohamed, An intelligent hybrid wavelet-adversarial deep model for accurate prediction of solar power generation, Energy Rep. 7 (2021) 2155–2164.
[29] Y. Zhang, A. Schlueter, C. Waibel, SolarGAN: Synthetic annual solar irradiance time series on urban building facades via Deep Generative Networks, Energy AI 12 (2023) 100223.
[30] G. Andrianakos, D. Tsourounis, S. Oikonomou, D. Kastaniotis, G. Economou, A. Kazantzidis, Sky image forecasting with Generative Adversarial Networks for cloud coverage prediction, in: 2019 10th International Conference on Information, Intelligence, Systems and Applications, IISA, IEEE, 2019, pp. 1–7.
[31] M. Sengupta, Y. Xie, A. Lopez, A. Habte, G. Maclaurin, J. Shelby, The national solar radiation data base (NSRDB), Renew. Sustain. Energy Rev. 89 (2018) 51–60.
[32] M. Sengupta, A. Weekley, A. Habte, A. Lopez, C. Molling, Validation of the National Solar Radiation Database (NSRDB)(2005–2012), Tech. Rep., National Renewable Energy Lab.(NREL), Golden, CO (United States), 2015.
[33] M. Sengupta, A. Habte, P. Gotseff, A. Weekley, A. Lopez, C. Molling, A. Heidinger, Physics-Based GOES Satellite Product for Use in NREL's National Solar Radiation Database, Tech. Rep., National Renewable Energy Lab.(NREL), Golden, CO (United States), 2014.
[34] P. Ineichen, R. Perez, A new airmass independent formulation for the Linke turbidity coefficient, Sol. Energy 73 (3) (2002) 151–157.
[35] J.-M. Montero, G. Fernández-Avilés, J. Mateu, Spatial and Spatio-Temporal Geostatistical Modeling and Kriging, John Wiley & Sons, 2015.

[36] I. Goodfellow, J. Pouget-Abadie, M. Mirza, B. Xu, D. Warde-Farley, S. Ozair, A. Courville, Y. Bengio, Generative adversarial nets, Adv. Neural Inf. Process. Syst. 27 (2014).
[37] A.X. Lee, R. Zhang, F. Ebert, P. Abbeel, C. Finn, S. Levine, Stochastic adversarial video prediction, 2018, arXiv preprint arXiv:1804.01523.
[38] M. Mathieu, C. Couprie, Y. LeCun, Deep multi-scale video prediction beyond mean square error, 2015, arXiv preprint arXiv:1511.05440.
[39] J. Marcos, L. Marroyo, E. Lorenzo, D. Alvira, E. Izco, Power output fluctuations in large scale PV plants: one year observations with one second resolution and a derived analytic model, Prog. Photovolt., Res. Appl. 19 (2) (2011) 218–227.